

See discussions, stats, and author profiles for this publication at: <https://www.researchgate.net/publication/261440528>

# Synthesis and multi-technique characterization of nickel loaded MCM-41 as potential hydrogen-storage materials

ARTICLE *in* MICROPOROUS AND MESOPOROUS MATERIALS · JUNE 2014

Impact Factor: 3.45 · DOI: 10.1016/j.micromeso.2014.03.005

---

CITATIONS

3

---

READS

51

7 AUTHORS, INCLUDING:



[Andrés Alberto García Blanco](#)

Universidad Nacional de San Luis

9 PUBLICATIONS 62 CITATIONS

SEE PROFILE



[Karim Sapag](#)

Universidad Nacional de San Luis

87 PUBLICATIONS 1,214 CITATIONS

SEE PROFILE

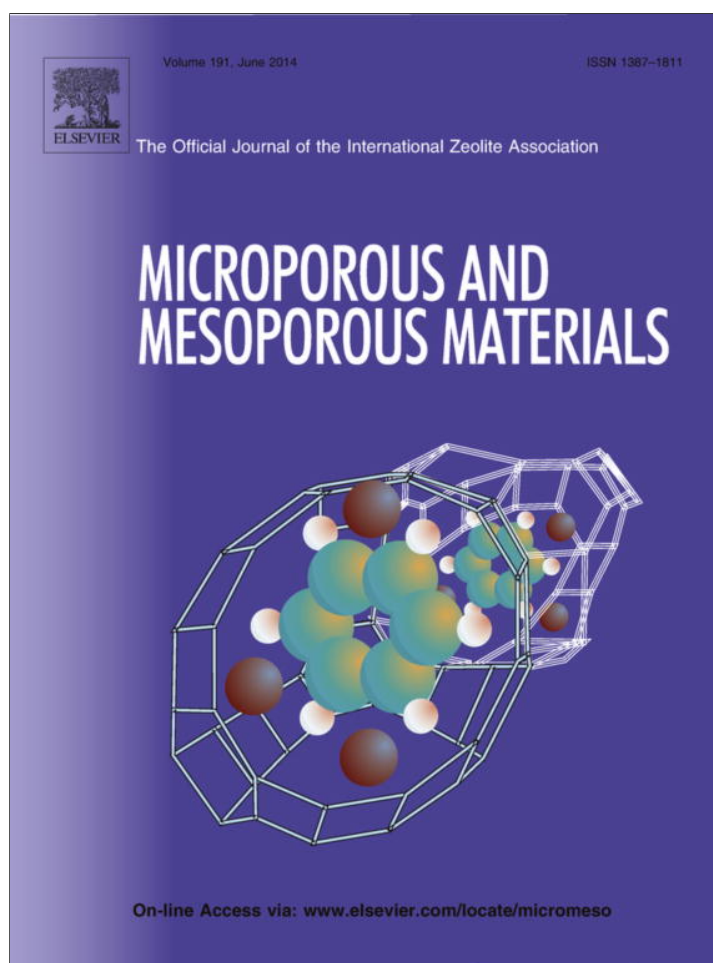


[Marcos Oliva](#)

National University of Cordoba, Argentina

27 PUBLICATIONS 129 CITATIONS

SEE PROFILE



This article appeared in a journal published by Elsevier. The attached copy is furnished to the author for internal non-commercial research and education use, including for instruction at the authors institution and sharing with colleagues.

Other uses, including reproduction and distribution, or selling or licensing copies, or posting to personal, institutional or third party websites are prohibited.

In most cases authors are permitted to post their version of the article (e.g. in Word or Tex form) to their personal website or institutional repository. Authors requiring further information regarding Elsevier's archiving and manuscript policies are encouraged to visit:

<http://www.elsevier.com/authorsrights>



Contents lists available at ScienceDirect

## Microporous and Mesoporous Materials

journal homepage: [www.elsevier.com/locate/micromeso](http://www.elsevier.com/locate/micromeso)

## Synthesis and multi-technique characterization of nickel loaded MCM-41 as potential hydrogen-storage materials

P. Carraro<sup>a,b</sup>, V. Elías<sup>b</sup>, A. García Blanco<sup>c</sup>, K. Sapag<sup>c</sup>, S. Moreno<sup>d</sup>, M. Oliva<sup>a</sup>, G. Eimer<sup>b,\*</sup><sup>a</sup> IFEG – CONICET, Universidad Nacional de Córdoba, Córdoba, Argentina<sup>b</sup> CITeQ – CONICET, Universidad Tecnológica Nacional-Facultad Regional Córdoba, Córdoba, Argentina<sup>c</sup> Laboratorio de Sólidos Porosos, INFAP – CONICET, Universidad Nacional de San Luis, San Luis, Argentina<sup>d</sup> Centro Atómico Bariloche, San Carlos de Bariloche, Argentina

## ARTICLE INFO

## Article history:

Received 17 December 2013

Received in revised form 27 February 2014

Accepted 1 March 2014

Available online 12 March 2014

## Keywords:

MCM-41

Nickel

Hydrogen storage

## ABSTRACT

Ni/MCM-41 samples have been successfully prepared by wet impregnation method with different degrees of metal loading. Various techniques including X-ray diffraction, N<sub>2</sub> adsorption–desorption, transmission electron microscopy, inductively coupled plasma atomic emission spectroscopy, electron microprobe analysis, UV–Vis diffuse reflectance spectra, infrared analysis, adsorption of pyridine coupled to infrared spectroscopy and hydrogen adsorption at 77 K at high and low pressure conditions were employed for the materials characterization. The Ni loading degree had a marked influence on the structural, chemical, acid and hydrogen storage properties of the samples. Thus, a low Ni loading favors the presence of highly dispersed Ni species responsible of the Lewis acidity. These species would promote hydrogen-favorable sites leading to a positive effect on the hydrogen storage capacity.

© 2014 Elsevier Inc. All rights reserved.

## 1. Introduction

Hydrogen, since long, has been proved to be the most ideal fuel to replace fossil fuels because it is a source of clean and efficient energy. It is lightweight, highly abundant and has high heating value with emission, during combustion, of an environmentally benign product as is water instead of carbon dioxide. However, there are major scientific challenges to overcome before the technology necessary to change from petroleum to hydrogen as an energy carrier can be implemented [1,2]. Hydrogen storage is the main problem to be conquered for the successful implementation of fuel cell technology in transport applications and it represents a major materials science challenge. Currently, many methods to store hydrogen, including high pressure gas, liquid hydrogen, adsorption on porous materials, metal hydrides and hydrogen intercalation in metals, are under consideration [3–5]. None of these methods completely satisfy all the criteria for the amount of hydrogen that can be supplied from a given weight or volume of tank for transport purposes. Nevertheless, the hydrogen physisorption on porous materials (such as carbons, metal–organic frameworks, polymers and zeolites) is one of the main methods being considered for vehicle applications, that permits storage of

large amounts at ambient temperatures [6–9] and safe pressures. In this sense, the interaction of hydrogen physisorbed within pores needs to be studied and understood in order to optimize porous materials for this application. On the other hand, it has been found that doping such porous solids with metals such as platinum, palladium and nickel leads to a hydrogen spillover effect where hydrogen molecules dissociate on the surface metal and hydrogen atoms diffuse inside the support, increasing the amount of hydrogen adsorbed [10–12]. Thus, a new family of micelle-templated mesoporous molecular sieves known as MCM-41 has recently been proposed as a potential new hydrogen storage material when they are modified with transition metals [13,14]. MCM-41 presents regular pore diameters between 2 and 10 nm, large surface areas (>1000 m<sup>2</sup>/g), well-defined mesoporous array and good adsorption properties. Moreover, MCM-41 is considered to be a suitable support for exploiting the hydrogen spillover effect since mesoporous materials can accommodate metallic nano-species of very high adsorption properties. Thus, Park et al. [14] have founded that the presence of nickel on MCM-41, prepared by hydrothermal process, creates hydrogen favorable sites that enhance the hydrogen storage capacity by spillover effect at 298 K and 100 bars. Meanwhile, Sheppard et al. [15] have presented hydrogen adsorption experiments at 77 K on mesoporous materials doped with Zn, where Zn low loadings favored the hydrogen storage with respect to MCM-41 pure. Prasanth et al. [13] have reported hydrogen

\* Corresponding author. Tel.: +54 3514690585.

E-mail address: [geimer@scdt.fr.utn.edu.ar](mailto:geimer@scdt.fr.utn.edu.ar) (G. Eimer).

adsorption studies on transition metals containing mesoporous materials at 77 K/1 bar and 300 K/40 bar. Ramachandran et al. [16] have evaluated the feasibility and perspectives of Al-MCM-41 impregnated with NiO, as hydrogen storage systems; finding that the hydrogen adsorption in Al-MCM-41 is strongly depend on density of Brønsted acid sites and the amount of metal oxide, especially NiO. Wu et al. [17] have presented hydrogen sorption experiments at 77 K/1 bar on MCM-41 materials doped with  $\text{Ni}^{2+}$ ,  $\text{Fe}^{3+}$ ,  $\text{Co}^{2+}$  and  $\text{Cr}^{3+}$  ions prepared under microwave irradiation, finding that only the presence of small amount of  $\text{Ni}^{2+}$  ions improved the hydrogen storage capacity. Recently, Yamamoto et al. [18] have reported the temperature dependence on the hydrogen adsorption properties, at pressures up to 1 bar at 298, 373, and 473 K, of nickel-doped mesoporous silica synthesized by a direct hydrothermal method. They observed that the hydrogen chemical adsorption increased with increasing nickel content and adsorption temperature. Nevertheless, although a few mesoporous materials (mainly PMOs) have been developed and tested in recent years for hydrogen storage at 77 K and high pressures, up to our knowledge there are not reports about MCM-41 for hydrogen storage at these conditions.

On the other hand, normally, both physical and chemical properties of the support, its acidity, reducibility and the extent of interaction with the active metal play important roles in the complex chemistry of supported metal catalysts. Nevertheless, a key objective is to find the appropriate metal and amount for modify the MCM-41 and to evaluate the relation between the obtained metallic species and the support that permits to improve their hydrogen storage capacity.

In this work, MCM-41 mesoporous materials impregnated with different levels of nickel were synthesized and exhaustively characterized by different instrumental techniques. Special emphasis was paid in the influence of the metal content on the structural, textural, chemical, acid properties of the samples and their relation with the hydrogen adsorption behavior at 77 K and high pressures.

## 2. Materials and methods

### 2.1. Synthesis

The pure siliceous mesoporous material (MCM-41) was synthesized as previously reported [19] following the method B, using cetyltrimethylammonium bromide (CTAB) as template, tetraethoxysilane (TEOS) (Aldrich 98%) as silicon source and sodium hydroxide (NaOH) aqueous solution 2 mol/L for hydrolysis and pH adjustment. The molar composition of gel was:  $\text{NaOH}/\text{Si} = 0.50$ ,  $\text{surfactant}/\text{Si} = 0.12$ ,  $\text{water}/\text{Si} = 132$ . In a usual synthesis, CTAB was dissolved in water–NaOH solution at 313 K; this new solution was then cooled to room temperature and TEOS was finally incorporated. The mixture was vigorously stirred for 4 h at room temperature and then for 3 h at 343 K in a closed flask. The final solid was filtered, washed and dried at 333 K overnight. To remove the template, the samples were heated (heating rate of 2 K/min) under  $\text{N}_2$  flow up to 773 K for 6 h and then calcined at the same temperature under air flow for 6 h.

Ni/MCM-41 molecular sieves were modified with different Ni loadings (1–15 wt.%) by the wet impregnation method. Firstly, 0.75 g of solid material (MCM-41), previously calcined at 773 K for 5 h, was added to 37.5 ml of an aqueous solution of  $\text{Ni}(\text{NO}_3)_2 \cdot 6\text{H}_2\text{O}$  with a concentration corresponding to the desired metallic loading. Then, the water was slowly removed by rotary evaporation at 323 K for about 30 min. The resulting powder was dried at 333 K and then calcined for 9 h at 773 K. The resulting materials were named Ni/MCM-41(x), where x indicates the expected metal loading percentage (nominal loading).

### 2.2. Characterization

The X-ray diffraction (XRD) patterns were recorded in a Philips PW 3830 diffractometer with  $\text{Cu K}\alpha$  radiation ( $\lambda = 1.5418 \text{ \AA}$ ) in the range of  $2\theta$  from 1.5 to  $7^\circ$  and from 10 to  $80^\circ$ . The interplanar distance ( $d_{100}$ ) was estimated using the position of the first X-ray diffraction line. The lattice parameter ( $a_0$ ) of the hexagonal unit cell was calculated as  $a_0 = (2/\sqrt{3}) d_{100}$ . A profile fitting was made to each maximum in the high angle range, and the mean grain size  $[D]$  of the corresponding phase was estimated using the Scherrer formulae:  $[D] = 0.9\lambda/\beta\cos\theta$ , where  $\beta$  (in radians) is the peak width at half maximum after subtraction of the instrumental contribution,  $\lambda$  is the X-ray wavelength and  $\theta$  the diffraction (Bragg) angle. The Ni content was determined by Inductively Coupled Plasma Atomic Emission Spectroscopy (ICP) using a spectrophotometer VISTA-MPX CCD Simultaneous ICP-OES-VARIAN. The surface elemental Energy-dispersive X-ray analysis was determined by electron microprobe analysis with energy dispersive spectrometry (EMPA-EDS) in an electron microprobe Jeol JXA 8230. The specific surface, the pore size distribution and the total pore volume ( $V_{\text{TP}}$ ) were determined from  $\text{N}_2$  adsorption–desorption isotherms obtained at 77 K using a Micromeritics ASAP 2000. The samples were previously degassed at 573 K for 12 h. The specific surface was calculated by the Brunauer–Emmett–Teller (BET) method in the pressure range of  $P/P_0$ : 0.01–0.25. The pore size distributions were determined by NLDFT method. Transmission electron microscopy (TEM) images were obtained using a Philips CM200UT transmission electron microscope. Samples were prepared by suspending the catalyst in ethyl alcohol 99.5% and casting a drop of the suspension onto a lacey carbon copper grid. The UV–Vis diffuse reflectance spectra (UV–Vis DRS) were recorded in air at room temperature using a Jasco 650 spectrometer with an integrating sphere in the wavelength range of 200–900 nm. The data were automatically transferred according to the Kubelka–Munk equation:  $f(R) = (1 - R_\infty)^2/2R_\infty$ . Infrared analysis of the Ni/MCM-41 samples was recorded on a Jasco 5300 FT-IR spectrometer. The IR spectra were obtained at room temperature in the range between 400 and  $1400 \text{ cm}^{-1}$  (lattice vibration region) using KBr 0.05% pellet technique. In order to evaluate the strength and type of acid sites, FT-IR spectral measurements of pyridine adsorption on the samples were also performed through the following procedure: Self-supported pellets of the samples ( $\sim 20 \text{ mg}$  and  $13 \text{ mm}$  of diameter) were prepared, placed in a thermostated cell with  $\text{CaF}_2$  windows connected to a vacuum line and evacuated for 7 h at 673 K under a dynamic vacuum; residual pressure was smaller than  $10^{-3} \text{ Pa}$ . The background spectrum was recorded first after cooling the sample to room temperature. Afterwards, the solid pellet was exposed to pyridine vapors (Sintorgan, 99% purity) until saturate the system to 46 mm Hg at room temperature; the contact time at this pressure was 12 h. After an IR spectrum of the adsorbed pyridine at room temperature was recorded, the subsequent IR spectra were obtained following the pyridine desorption by evacuation for 1 h at 323, 373 and 473 K. Finally, the difference spectrum for each sample was obtained by subtracting the background previously recorded. Hydrogen (99.995%) adsorption capacity at 77 K and pressures up to 10 bar were measured in an automated nanometric system ASAP 2050 (Micromeritics Instrument Corporation). Previous to all the adsorption experiments, the samples were degassed at 573 K during 12 h under vacuum conditions ( $5 \times 10^{-3} \text{ mm Hg}$ ).

## 3. Results and discussion

X-ray diffraction is one of the most important techniques for characterizing the structure of crystalline or other ordered materials. It has been widely used in the study of MCM-41 materials to

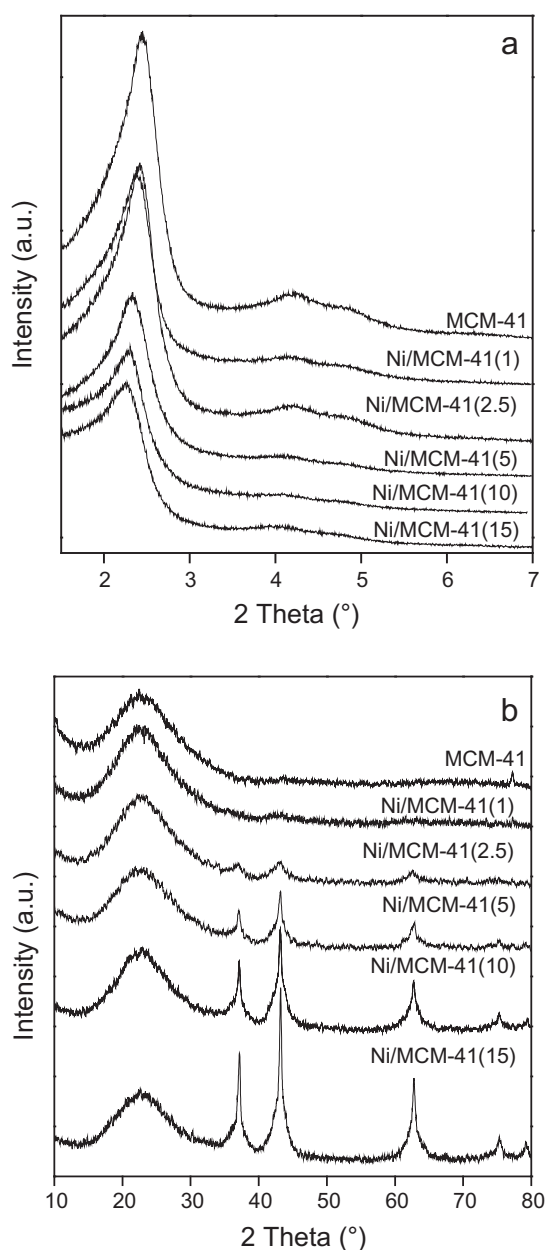


Fig. 1. Low-angle XRD patterns (a) and high-angle XRD patterns of samples (b).

complement the nitrogen physisorption because of its capability of assessing the hexagonal structure of the samples. The low-angle XRD patterns of the materials synthesized in this study are shown

in Fig. 1a. Three diffraction peaks are clearly observed for the MCM-41, indexed as (100), (110) and (200) reflections, characteristic of a highly ordered mesoporous structure with hexagonal pore array [20]. The low angle XRD patterns of the nickel loaded samples are similar to that of the pure MCM-41, indicating that the structure was preserved after nickel loading. Thus, this structure allowed an actual Ni loading of up to  $\approx 10$  wt.% without collapsing. However, increasing actual nickel loading from  $\sim 4$  to 10 wt.% (corresponding to nominal loadings from 5 to 15 wt.%; see Table 1), the peaks are broadened and the (100) and (200) reflections appear less defined, which indicates a loss of periodicity concerning to the mesopores.

Fig. 1b shows the high-angle XRD patterns of the Ni/MCM-41 samples in order to assess the crystallinity of the Ni oxide loaded onto the support. All of the patterns exhibited the broad amorphous silica peak at around  $23^\circ$ . In addition, the Ni/MCM-41(15) sample showed four narrow and intense peaks at  $2\theta = 37^\circ$ ,  $43^\circ$ ,  $64^\circ$  and  $75^\circ$ , which are assigned to the presence of crystalline nickel oxide (NiO) [21]. Ni/MCM-41(10) and Ni/MCM-41(5) exhibited broader and weaker diffraction peaks at similar positions, indicating the presence of smaller NiO particles. The mean crystallite sizes of NiO, estimated by the Scherrer equation, were  $11 \pm 3$ ,  $7 \pm 4$  and  $3 \pm 1$  nm for the Ni/MCM-41(15), Ni/MCM-41(10) and Ni/MCM-41(5) samples respectively. The other samples with lower Ni loadings show only hints of the mentioned peaks, which suggests that the oxides are in amorphous state or are clusters/particles too small to be accurately determined by XRD. On the other hand, as it can be observed through the relative areas of the peaks, a higher Ni loading favors the major formation of oxide particles on the surface of solids.

$N_2$  adsorption–desorption isotherms with their corresponding pore size distribution of the Ni/MCM-41 and MCM-41 samples are shown in Fig. 2; the corresponding physical parameters are collected in Table 1. All the samples exhibited type IV isotherms, typical of mesoporous structures, which present hysteresis loops with parallel and almost horizontal branches, classified as H4-type according to IUPAC. Moreover, all samples exhibited a distinct inflection in the  $P/P_0$  range from 0.1 to 0.25, characteristic of a narrow step of capillary condensation inside the mesopores. This feature provides evidence of narrow pore size distribution curves that indicate the uniformity of pore arrangement. These results are in agreement with those previously reported by us [22,23]. However, whereas the inflection is sharp for the MCM-41 (giving account for the narrow pore size distribution), it becomes less pronounced with metal loading increasing, which indicates a bigger range in the distribution of the pore sizes ( $D_p$ ) and accords with the decrease of structural order detected by XRD. In addition, all the samples showed high specific surface and pore volume ( $V_{TP}$ ), which are typical of mesoporous materials; nevertheless, a slight decrease in these values is observed with Ni loading increasing. Thus, the increased presence of clusters and/or small particles of

**Table 1**  
Structure properties and chemical composition of the synthesized samples.

Sample	Area ( $m^2/g$ ) <sup>a</sup>	$a_0$ (nm)	Ni content (wt.%) <sup>b</sup>	Ni content (wt.%) <sup>c</sup>	$D_p$ (nm) <sup>d</sup>	$V_{TP}$ ( $cm^3/g$ ) <sup>d</sup>	$t_w$ (nm) <sup>e</sup>
MCM-41	940	4.16	–	–	3.5	0.70	0.667
Ni/MCM-41(1)	910	4.25	0.81	0.83	3.2	0.56	1.052
Ni/MCM-41(2.5)	860	4.23	2.16	2.33	3.2	0.54	1.031
Ni/MCM-41(5)	825	4.37	4.01	4.13	3.2	0.53	1.174
Ni/MCM-41(10)	695	4.45	8.01	8.75	3.3	0.46	1.152
Ni/MCM-41(15)	695	4.50	11.34	10.54	3.2	0.41	1.308

<sup>a</sup> Determined by BET.

<sup>b</sup> Determined by ICP.

<sup>c</sup> Determined by EPMA-EDS.

<sup>d</sup> Pore diameter ( $D_p$ ) and pore volume ( $V_{TP}$ ) determined by  $N_2$  adsorption–desorption.

<sup>e</sup> Pore wall thickness:  $t_w = a_0 - D_p$ .



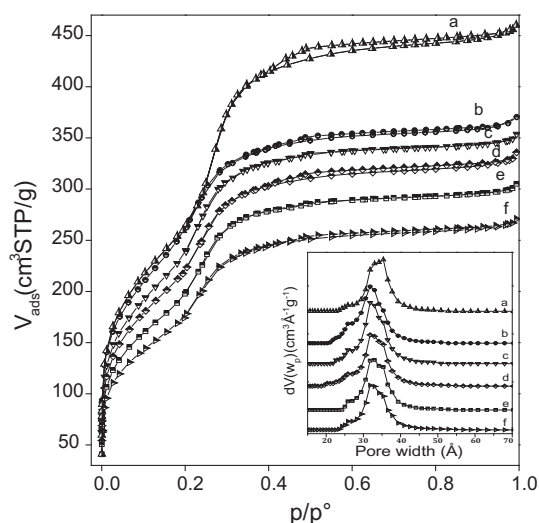


**Fig. 2.** Nitrogen adsorption–desorption isotherms and NLDFT pore size distribution (inset) of (a) MCM-41, (b) Ni/MCM-41(1), (c) Ni/MCM-41(2.5), (d) Ni/MCM-41(5), (e) Ni/MCM-41(10) and (f) Ni/MCM-41(15).

metal oxides finely dispersed inside the channels as well as large particles (detectable by XRD) on the external surface could affect the pore structure provoking the observed behavior. In fact, the growth of bigger oxides particles on the external surface of the samples, promoted by the highest Ni loading, could cause the blocking of some pores, the high structural deterioration and consequently the highest decrease in the values of specific surface and pore volume. Finally, a pore wall thickness ( $t_w$ ) increase is observed when Ni loading is increased, which could give evidence

of an increasing amount of different Ni species inside the channels. Thus, the variation in the different parameters allowed us infer about the presence of nickel species inside the pores of mesoporous framework. However, the high pore volume (Fig. 2 and Table 1) suggests that the void space in the mesoporous host is open for the entry of hydrogen, although a small portion of the channels may be stuck with clusters or nanoparticles of nickel oxide. This void space is very important for that the hydrogen molecule can diffuse into the silica matrix and interact with the metallic species inside the pores [13].

Figs. 3 and 4 show the transmission electron microscopy images (TEM) of the synthesized samples. The images exhibit well-ordered parallel straight mesochannels, characteristic of the regular and hexagonal pore arrangement of MCM-41 type materials, which was also inferred from the XRD patterns. Figs. 3a<sub>1</sub>, b<sub>1–2</sub> and 4a<sub>1</sub>, b<sub>1–2</sub>, c<sub>1</sub> mainly correspond to views perpendicular to the direction of the pore arrangement, where it can be observed straight channels arranged along the long axis; meanwhile the hexagonal arrangement of unidirectional mesopores is clear in Figs. 3a<sub>1–2</sub>, b<sub>1–2</sub>, and 4a<sub>1–2</sub>, b<sub>2</sub> and c<sub>1–2</sub> which show frontal views of them. The pore size estimated from TEM images is about 3.3 nm, which is close to that obtained from N<sub>2</sub> adsorption–desorption isotherms. On the other hand, this study also reveals the size distribution of the Ni oxides formed on the solids. Since darker areas in TEM images represent the electronically more dense phases, metal oxide is considered to be present when irregular contrasts in the images are observed [24]. Thus, high-contrast regions, extended over more than one pore, that randomly interrupt the pore arrangement characteristic of the mesoporous materials can be attributed to the presence of NiO. These areas, corresponding to Ni oxide particles segregated on the external surface of the silicate [24], are mainly observed for the samples with higher Ni loadings (Fig. 3) in agreement with the peaks assigned to these oxides in the

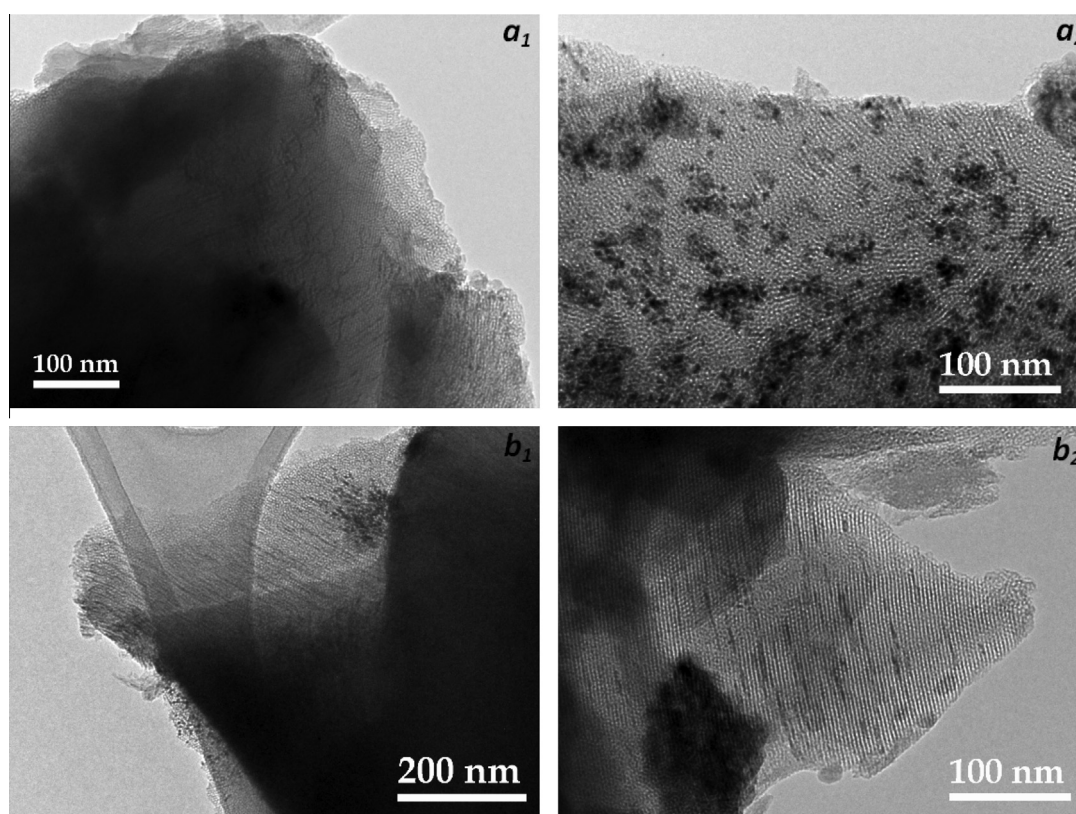


**Fig. 3.** Transmission electron microscopy images of (a) Ni/MCM-41(15) and (b) Ni/MCM-41(10).

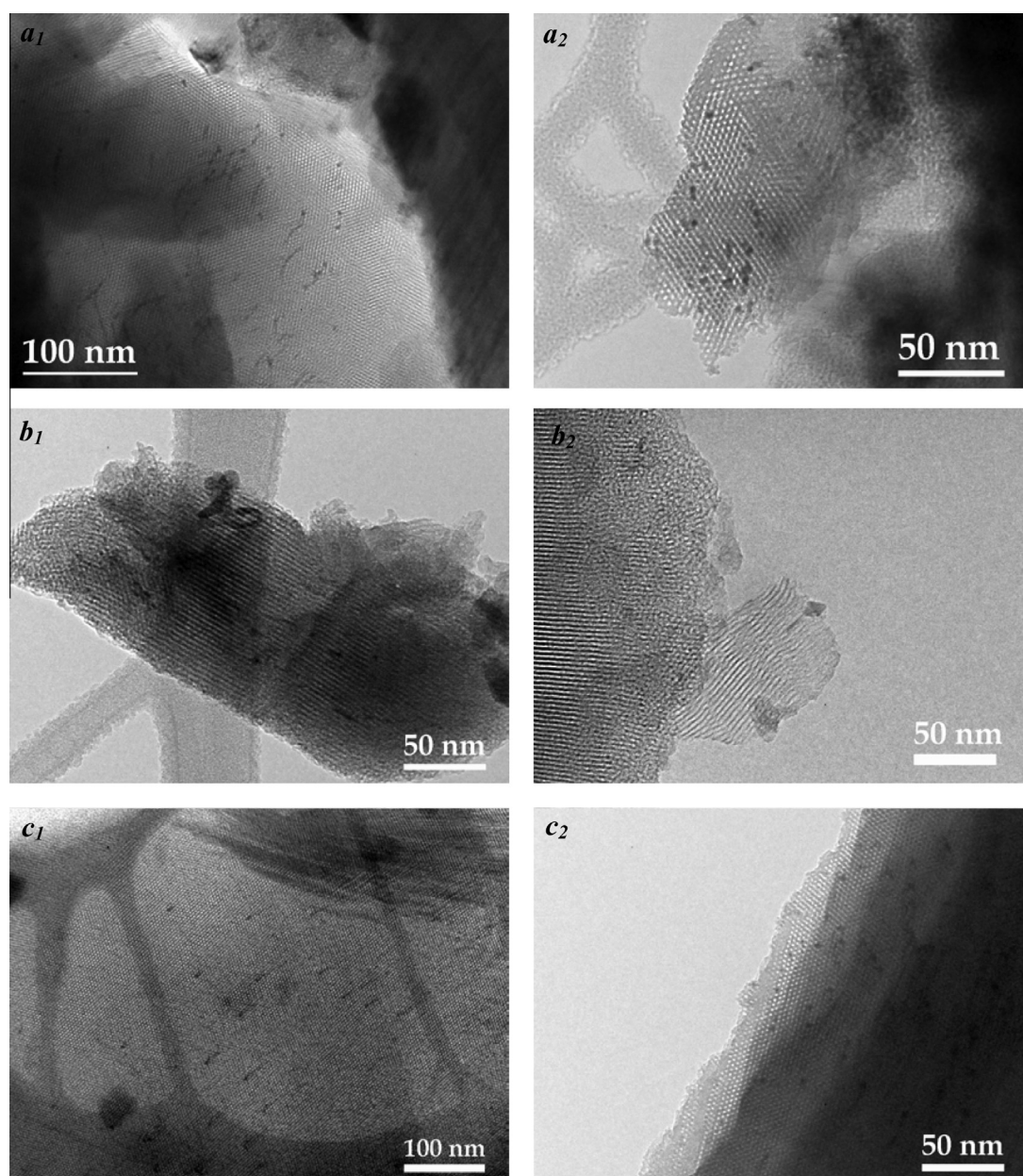


Fig. 4. Transmission electron microscopy images of (a) Ni/MCM-41(5), (b) Ni/MCM-41(2.5), and (c) Ni/MCM-41(1).

XRD analysis. These particles, with sizes of around 3–12 nm, appear also to be aggregated into larger secondary particles of around 20–30 nm. This feature is expected for materials modified with transition metals prepared by wet impregnation. On the other hand, it can be also inferred that the nickel oxide is located inside the pores due to that small black spots, which have a size of the order of the pore size, are isolated and are filling one pore while its neighbors are empty [24]. This is observed even for the sample with the lower Ni loading (Fig. 4c<sub>2</sub>). Moreover, the incorporation of the nickel oxide inside the mesoporous channels, as clusters or very small nanoparticles, is also evidenced by the darker regions along the mesopores that are increased with the Ni loading (see Figs. 3a<sub>1</sub>, b<sub>1–2</sub> and 4a<sub>1</sub>, b<sub>1</sub>, c<sub>1</sub>). This behavior was already observed in samples modified with chromium with similar metal contents and synthesized by the same impregnation method [25–27].

UV–Vis DRS spectroscopy is a useful method to characterize the coordination environment of transition metals that are incorporated into the mesoporous materials. In this paper, this method

is also used to infer about the presence of different Ni species on the synthesized mesoporous samples. The UV–Vis DRS spectra of the MCM-41 samples and a NiO reference sample are shown in Fig. 5. The main feature for all of the samples is an intense absorption in the UV region. This band, that appear in the 250–350 nm range, is typically associated to the  $O^{2-}(2p) \rightarrow Ni^{2+}(3d)$  charge transfer transition of octahedral  $Ni^{2+}$  species in NiO lattices [29]. This absorption increases in intensity and its position shifts to higher wavenumber with increasing Ni loading. It is known that the position of the absorption edge of semiconductor powders is strongly affected by particle size shifting significantly to lower wavelength by decreasing particle size. Accordingly, depending on shape and size of the NiO particles, the absorption in the UV region is reported to change in shape and position [28,29]. Therefore, the shifting of the UV band position observed suggests that the NiO clusters or nanoparticles predominant in the samples with higher Ni loadings should be larger and probably of weaker interaction with the matrix. This agrees with the NiO crystallite sizes



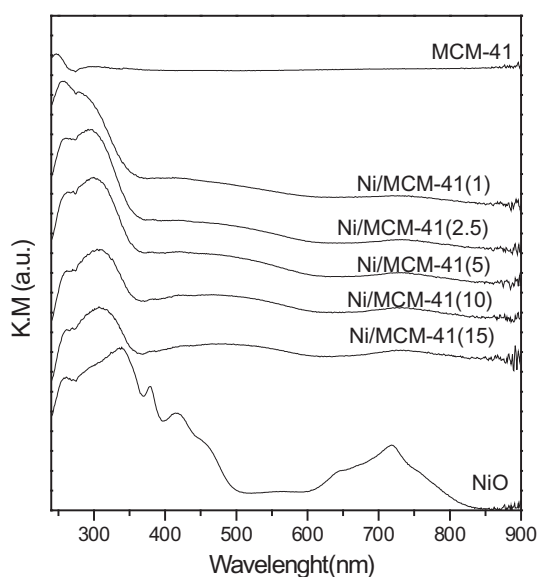


**Fig. 5.** DRUV-vis spectra of NiO reference and the MCM-41 synthesized samples with different Ni contents.

measured from XRD data. On the other hand, the samples with Ni loadings above 1 wt.% also show absorption bands at about 400–550 and 700–850 nm, which become stronger with increasing metal loading. These absorptions in the visible region are associated to several kinds of d–d transitions, superimposed each other, of  $\text{Ni}^{2+}$  ions in octahedral local environment in NiO. The last band, more noticeable for the highly loaded samples, has been related to octahedral  $\text{Ni}^{2+}$  in bulk NiO [30] indicating thus the presence of this phase [31]. In conclusion, this technique suggests that depending on the Ni loading, clusters or nanoparticles with a local structure similar to that of NiO but with different sizes and interactions with the matrix exist on our materials. The amount of these species as well as the presence of larger particles, probably with lower interaction with the mesoporous matrix, is increased by increasing the metal loading degree. Finally, the presence of isolated mononuclear  $\text{Ni}^{2+}$  species interacting with the mesoporous framework oxygen (related to a  $\text{O}^{2-} \rightarrow \text{Ni}^{2+}$  charge transfer transition in the mesoporous lattice that could be also associated with the band at 260 nm), should not be discarded.

The infrared spectra in the 400–1400  $\text{cm}^{-1}$  range for KBr-pelletized Ni/MCM-41 are shown in Fig. 6. Two bands at around 1080 and 1238  $\text{cm}^{-1}$  are associated to transverse-optical and longitudinal-optical modes of asymmetric Si–O stretching, meanwhile the bands at 460 and 800  $\text{cm}^{-1}$  are assigned to symmetric stretching and tetrahedral bending of Si–O bonds, respectively [32–33]. A characteristic band at 960  $\text{cm}^{-1}$  is also clearly observed in the spectra and can be interpreted in terms of the overlapping of both Si–OH and Si–O–Ni stretching vibrations [33]. In addition, a very slight shift of the band centered at 1080  $\text{cm}^{-1}$  toward lower wavenumbers according to Ni loading increasing may be attributed to an increase in the Si–O distance in the walls caused by the substitution of the smaller Si by the larger  $\text{Ni}^{2+}$  possibly in coordination with oxygen of silica framework [14].

In addition, usually a shift of the band centered at 1080  $\text{cm}^{-1}$  toward lower wavenumbers may be attributed to an increase in the Si–O distance in the walls caused by the substitution of the smaller Si by the larger  $\text{Ni}^{2+}$  in coordination with oxygen of silica framework [14]. Nevertheless, the shift of this band observed for our samples seems too small to allow us to affirm the substitution of Si by Ni. In this sense, the Ni incorporation into the framework is not expected given the used synthesis method in this work.

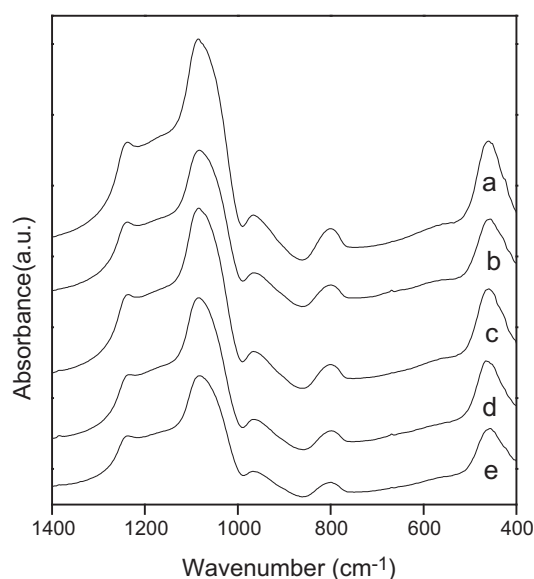


**Fig. 6.** FT-IR spectra in the 400–1400  $\text{cm}^{-1}$  range of (a) Ni/MCM-41(1), (b) Ni/MCM-41(2.5), (c) Ni/MCM-41(5), (d) Ni/MCM-41(10) and (e) Ni/MCM-41(15).

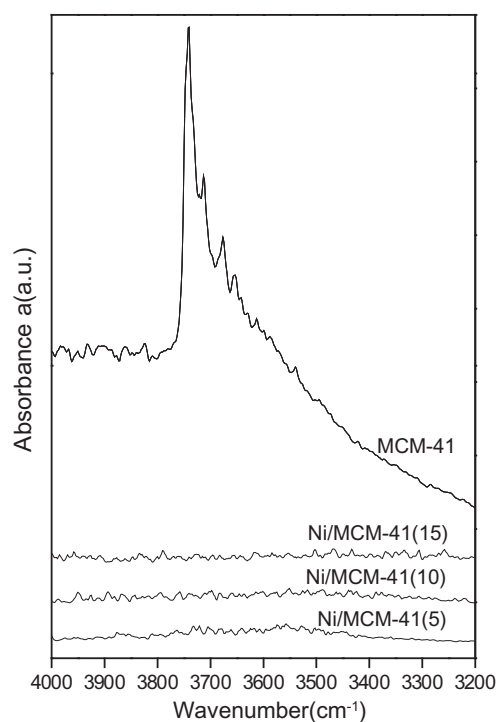


**Fig. 7.** FT-IR spectra in the 4000–3200  $\text{cm}^{-1}$  range of some synthesized samples.

The IR spectra in the hydroxyl range of the MCM-41 and the Ni/MCM-41 samples, previously degassed at 673 K for 7 h, are compared in Fig. 7. The spectrum of MCM-41 shows a band at approximately 3740  $\text{cm}^{-1}$  assigned to the O–H stretching vibrations of terminal silanols groups [37]. For the Ni/MCM-41 samples this band became invisible likely due to the coordination of the Si–OH groups with Ni ions giving rise to Si–O–Ni bonds. This feature has been already observed by us elsewhere [37], where we suggested that Si–OH groups could be blocked after the condensation with Cu species, leading to the formation of Si–O–Cu bonds.

The chemisorption of pyridine followed by IR studies is usually a useful probe to detect the presence and nature of acid sites on a



catalyst surface [34]. The pyridine, as basic molecule, can interact via the nitrogen lone-pair electrons with these acid sites, giving rise to characteristic bands. Information on the strength of Lewis and Brønsted acid sites can be obtained from pyridine thermodesorption. IR spectra of pyridine adsorbed on MCM-41 and Ni/MCM-41 samples and desorbed at 323, 373 and 473 K for an hour are shown in Fig. 8. Note that in order to make a semi quantitative and comparative analysis, all of the curves were affected by the pellet mass. It is known that pyridine forms hydrogen bonds with the silanol groups present in the structure whose hydroxyls are not capable to protonate pyridine. Thus, bands corresponding to hydrogen-bonded pyridine at  $1446$  and  $1596\text{ cm}^{-1}$  [34–36] are the only bands found in pure MCM-41, which disappear upon evacuation at  $473\text{ K}$  indicating the weak interaction between pyridine and the SiOH groups. However, according to the literature and to our previous reports [34–39] the formation of a Lewis-type adduct with adsorbed pyridine is identified by IR absorption bands at about  $1600$ – $1620$  and  $1445$ – $1455\text{ cm}^{-1}$ . In this sense, the presence of these bands at  $1446$  and  $1596\text{ cm}^{-1}$  also in the Ni-modified samples could be interpreted in terms of the overlapping of both the hydrogen-bonded pyridine band and a band attributed to pyridine coordinately bonded to Lewis acid sites (Lewis-type adduct) [40–44]. Nevertheless, according to the results obtained for the OH adsorption region, for these samples the Si–OH groups would be likely blocked after the condensation with the Ni species (Si–O–Ni bonds). Therefore, the presence of the bands mentioned at  $1446$  and  $1596\text{ cm}^{-1}$  in Ni-impregnated samples could be only attributed to the formation of a strong “electron-donor–acceptor” adduct of pyridine–Lewis sites, probably due to an interaction between a Ni unoccupied molecular orbital and the probe molecule. Thus, these Lewis sites, enough strong to retain pyridine until  $473\text{ K}$  (Fig. 8C), could arise from the isolated nickel species coordinate to framework oxygen atoms. In this regard, the origin of such Lewis acidity in Cu-modified MCM-41 was studied by us elsewhere [37]. In addition, it is possible to observe in Fig. 8 that the signals become more intense according the Ni content is increased in the samples to a 4.13 wt.% (Ni/MCM-41(5)). Then, the signals are diminished for the higher Ni loadings. This behavior may be probably assigned to a blocking effect of larger Ni oxide clusters or particles (present in these samples) over the acid sites.

In order to corroborate the origin of such Lewis acidity, the acidity of the samples was again measured after a reduction treatment was performed. The employed reduction conditions ( $\text{H}_2$  flow =  $70\text{ ml/min}$ ;  $723\text{ K}$ ) allow a complete reduction of the NiO clusters or nanoparticles, according to temperature programmed reduction (TPR) analysis reported in [45,46]. Thus, the Fig. 8 also shows FT-IR spectra of some reduced samples, recorded after the adsorption of pyridine and subsequent evacuation at  $373\text{ K}$ . As it is observed, the spectra of the reduced samples are very similar to those from non-reduced samples. Therefore, this feature allows us to restate that the Lewis acid sites generated by the incorporation of nickel in the silica can be mainly attributed to the presence of highly dispersed nickel species coordinated to the framework oxygen, which cannot be reduced at  $723\text{ K}$ .

In order to analyze the capacity of the synthesized materials for the hydrogen storage, some representative samples were studied. The Fig. 9 shows the adsorption excess isotherms measured at  $77\text{ K}$  of the pure MCM-41 and the Ni modified MCM-41 sieves. It is important to note that hydrogen is a supercritical gas at the temperature of engineering interest and follows a different adsorption mechanism compared to the sub-critical gases. Usually, the excess isotherms tend to a maximum after which, the excess amount tends to diminish [5,47,48]. This maximum occurs at a point where the difference between the density of the adsorbed phase and that of bulk phase is maximal. Beyond this point, i.e. for higher pressures, the difference between these densities becomes smaller,

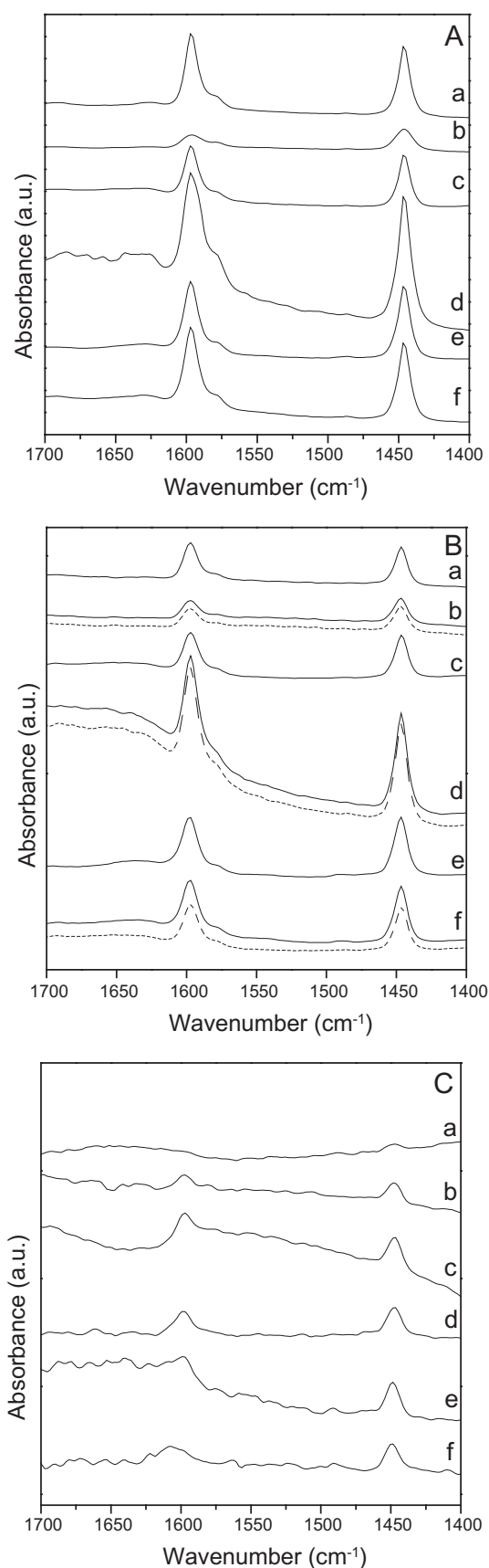


**Fig. 8.** FT-IR spectra of pyridine adsorbed on the synthesized samples: (a) MCM-41, (b) Ni/MCM-41(1), (c) Ni/MCM-41(2.5), (d) Ni/MCM-41(5), (e) Ni/MCM-41(10) and (f) Ni/MCM-41(15). Desorption at  $323\text{ K}$  (A),  $373\text{ K}$  (B) and  $473\text{ K}$  (C). The spectra of the corresponding reduced samples desorbed at  $373\text{ K}$  are shown in dashed lines.

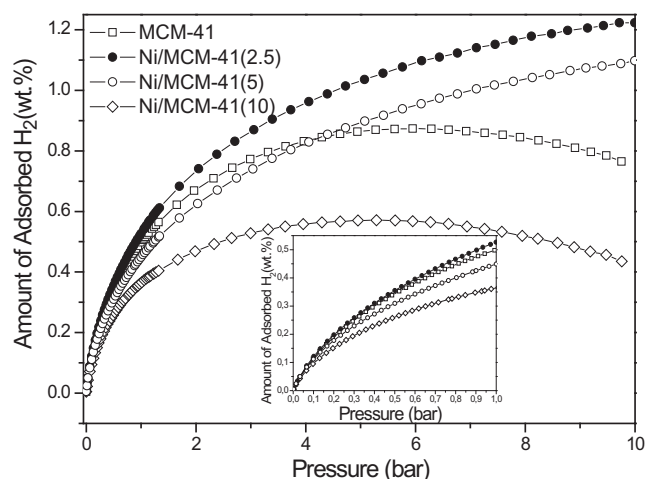


Fig. 9.  $H_2$  adsorption–desorption isotherms of the synthesized samples, measured at 77 K. Inserted figure shows the amplified region for low pressures.

consequently decreasing the excess amount. The position of this point depends basically on the adsorbate-adsorbent interaction as on the thermodynamic state of the adsorptive [55]. In the  $H_2$  excess isotherms measured, this maximum was observed for the MCM-41 and Ni/MCM-41(10) samples, but it was not observed for the samples with the lowest Ni loading. The Ni/MCM-41(2.5) sample presents a high capacity of  $H_2$  storage at 77 K, reaching a 1.23 wt.% around 10 bar, followed by the Ni/MCM-41(5) with a maximum of 1.10 wt.% at the same pressure. Meanwhile, the MCM-41 and Ni/MCM-41(10) samples shows a minor adsorption capacity, reaching a maximum of 0.88 and 0.57 wt.%, respectively, at 5–6 bar.

It is interesting to observe that, at low pressures (up to 1 bar), the samples modified with higher nickel loadings present lower hydrogen storage capacities than the MCM-41. Probably, the increased presence of different nickel species in the structure could be obstructing the access of hydrogen towards the channels. However, the slightly higher storage capacity observed for the sample with the lower Ni loading (Ni/MCM-41(2.5)) is giving account for some interaction between the  $H_2$  and nickel species finely dispersed on the MCM-41. This interaction between nickel and  $H_2$  could be produced even at high pressures, resulting in an increased hydrogen storage capacity of the nickel modified samples with respect to the MCM-41, even for a nominal nickel content of 5 wt.%. Thus, a low nickel loading on our MCM-41 materials have a positive effect on the hydrogen storage capacity, probably due to the highly dispersed Ni species, which would be promoting the presence of hydrogen-favorable sites [14,17]. According to the literature, a charge transfer from the metal to the support surface and a charge-induced dipole interaction could be taking place to keep together the Ni atoms and  $H_2$  molecules [14,49–51]. Thus, in our samples, isolated Ni species with Lewis acid character (which was inferred from adsorption of pyridine coupled to FT-IR) could polarize the  $H_2$  molecules on the surface, without charge transfer from  $H_2$  to the Ni atoms. Therefore, these highly dispersed acidic Ni species could interact with  $H_2$  at 77 K through the formation of  $Ni^{2+}\cdot H_2$  adducts, increasing the hydrogen storage capacity of the MCM-41 materials [13,52,53]. On the other hand, when the nickel loading is increased, a decrease in hydrogen adsorption capacity is observed. This fact could be due to both the gradual deterioration of the structure, evidenced by XRD, as well as to the decrease in the specific surface. Likewise, it is probably that the major formation of oxide clusters or NiO nanoparticles may

be avoiding the access of hydrogen towards the interior of channels. In concordance with our results Saha et al. and Zeilinski et al. [11,54] have reported that for nickel-doped carbons, the hydrogen adsorption is maximum at a low metal content and it then decreases with increasing nickel loading on the carbons.

#### 4. Conclusion

Ni/MCM-41 molecular sieves have been successfully prepared by wet impregnation with  $Ni(NO_3)_2\cdot 6H_2O$  as nickel source. All of the materials exhibited high specific surface, pore volume and structural regularity typical of the MCM-41 mesoporous materials. Whereas the incorporation of the nickel oxide inside the channels, as clusters or very small nanoparticles, was evidenced for all of the samples, the higher Ni loadings promoted the growth of bigger oxides particles on the external surface of the silicates. Thus, depending on the metal loading, our materials show Ni species with a local structure similar to that of NiO but with different sizes and interactions with the matrix. Moreover, the presence of isolated mononuclear Ni species, probably interacting with framework oxygen through its coordination with the SiOH groups, could also be inferred. These species, highly dispersed on the structure, would be the responsible of the Lewis acidity that present our samples. Meanwhile, a positive effect on the hydrogen storage capacity, observed for the samples with low Ni loading, could be also associated to the presence of these highly dispersed Ni species which could give rise to hydrogen favorable sites.

#### Acknowledgements

The authors are grateful to CONICET, UTN-FRC and FaMAF-UNC for the financial support and to LAMARX for EMPA analysis.

#### References

- [1] A. Züttel, *Mater. Today* 6 (2003) 24–33.
- [2] R. Coontz, B. Hanson, *Science* 305 (2004) 957 (Special issue).
- [3] P. Jena, *J. Phys. Chem. Lett.* 2 (2011) 206–211.
- [4] Michael Hirscher, *Handbook of Hydrogen Storage: New Materials for Future Energy Storage*, first., Wiley-VCH, Germany, 2010.
- [5] A. García Blanco, A. Vallone, A. Gil, K. Sapag, *Int. J. Hydrogen Energy* 37 (2012) 14870–14880.
- [6] S. Satyapal, J. Petrovic, C. Read, G. Thomas, G. Ordaz, *Catal. Today* 120 (2007) 246–256.
- [7] K. Mark Thomas, *Catal. Today* 120 (2007) 389–398.
- [8] B. Panella, M. Hirscher, S. Roth, *Carbon* 14 (2005) 2209–2214.
- [9] E. Poirier, A. Dailly, *Langmuir* 25 (20) (2009) 12169–12176.
- [10] W. Conner, J. Falconer, *Chem. Rev.* 95 (1995) 759–788.
- [11] D. Saha, S. Deng, *Langmuir* 25 (2009) 12550–12560.
- [12] R. Prins, *Chem. Rev.* 112 (2012) 2714–2738.
- [13] K. Prasanth, M. Raj, H. Bajaj, T. Kim, R. Jasra, *Int. J. Hydrogen Energy* 35 (2010) 2351–2360.
- [14] S. Park, S. Lee, *J. Colloid Interface Sci.* 346 (2010) 194–198.
- [15] D. Sheppard, C. Buckley, *Int. J. Hydrogen Energy* 33 (2008) 1688–1692.
- [16] S. Ramachandran, H. Jang-Hoon, D. Kyung Kim, *Catal. Commun.* 8 (2007) 1934–1938.
- [17] C. Wu, Q. Gao, J. Hu, Z. Chen, W. Shi, *Microporous Mesoporous Mater.* 117 (2009) 165–169.
- [18] Y. Yamamoto, N. Nawa, S. Nishimoto, Y. Kameshima, M. Matsuda, M. Miyake, *Int. J. Hydrogen Energy* 36 (2011) 5739–5743.
- [19] V. Elias, M. Crivello, E. Herrero, S. Casuscelli, G. Eimer, *J. Non-Cryst. Solids* 355 (2009) 1269–1273.
- [20] Y. Do, J. Kim, J. Park, S. Park, S. Hong, C. Suh, G. Lee, *Catal. Today* 101 (2005) 299–305.
- [21] D. Lensveld, J. Gerbrand Mesu, A. Dillen, K. Jong, *Microporous Mesoporous Mater.* 401–407 (2001) 44–45.
- [22] G. Eimer, C. Chanquia, K. Sapag, E. Herrero, *Microporous Mesoporous Mater.* 116 (2008) 670–676.
- [23] V. Elias, E. Sabre, K. Sapag, S. Casuscelli, G. Eimer, *Appl. Catal. A* 413–414 (2012) 280–291.
- [24] J. Bengoa, M. Cagnoli, N. Gallegos, A. Alvarez, L. Moggi, M. Moreno, S. Marchetti, *Microporous Mesoporous Mater.* 84 (2005) 153–160.
- [25] V. Elias, E. Sabre, E. Winkler, M. Satuf, E. Rodríguez-Castellón, S. Casuscelli, G. Eimer, *Microporous Mesoporous Mater.* 163 (2012) 85–95.

- [26] W. Wang, M. Song, Z. Zhang, M. Richardson, J. Non-Cryst. Solids 352 (2006) 2180–2186.
- [27] K. Choi, R. Wakabayashi, T. Tatsumi, T. Yokoi, K. Kuroda, J. Colloid Interface Sci. 359 (2011) 240–247.
- [28] V. Volkov, Z. Wang, B. Zou, J. Phys. Chem. Lett. 337 (2001) 117–124.
- [29] A. Tirsoaga, D. Visinescu, B. Jurca, A. Ianculescu, O. Carp, J. Nanopart. Res. 13 (2011) 6397–6408.
- [30] K. Hadjiivanov, M. Mihaylov, D. Klissurski, P. Stefanov, N. Abadjieva, E. Vassileva, L. Mintchev, J. Catal. 185 (1999) 314.
- [31] J. Escobar, J. De Los Reyes, T. Viveros, Appl. Catal. A 253 (2003) 151–163.
- [32] E.I. Kamitsos, A.P. Patsis, G. Kordas, Phys. Rev. B 48 (1993) 12499.
- [33] G. Eimer, S. Casuscelli, G. Ghione, M. Crivello, E. Herrero, Appl. Catal. A 298 (2006) 232–242.
- [34] V. Elías, M. Crivello, E. Herrero, S. Casuscelli, G. Eimer, Ind. Eng. Chem. Res. 48 (2008) 9076–9082.
- [35] E. Vaschetto, G. Monti, E. Herrero, S. Casuscelli, G. Eimer, Appl. Catal. A 453 (2013) 391–402.
- [36] G. Eimer, S. Casuscelli, C. Chanquia, V. Elias, M. Crivello, E. Herrero, Catal. Today 133–135 (2008) 639–646.
- [37] C. Chanquia, L. Andrini, J. Fernandez, M. Crivello, F. Requejo, E. Herrero, G. Eimer, J. Phys. Chem. C 114 (2010) 12221–12229.
- [38] T. Conesa, J. Hidalgo, R. Luque, J. Campelo, A. Romero, Appl. Catal. A 299 (2006) 224–234.
- [39] A. Jentys, K. Kleestorfer, H. Vinek, Microporous Mesoporous Mater. 27 (1999) 321–328.
- [40] B. Chakraborty, B. Viswanathan, Catal. Today 49 (1999) 253–260.
- [41] C. Otero Arèan, M. Rodriguez Delgado, V. Montouillout, J. Lavalley, C. Fernández, J. Cuart Pascual, J. Parra, Microporous Mesoporous Mater. 67 (2004) 259.
- [42] E. Escalona Platero, M. Peñarroya Mentrut, C. Otero Arèan, A.J. Zecchina, J. Catal. 162 (1996) 268.
- [43] C. Morterra, G. Magnacca, Catal. Today 27 (1996) 497.
- [44] L. Chen, L. Noeña, J. Navarrete, J. Wang, Mater. Chem. Phys. 97 (2006) 236.
- [45] Á. Szegedi, M. Popova, V. Mavrodinova, M. Urbán, I. Kiricsi, C. Minchev, Microporous Mesoporous Mater. 99 (2007) 149–158.
- [46] T. Klimova, M. Calderón, J. Ram, Appl. Catal. A 240 (2003) 29–40.
- [47] J. Moellmer, A. Moeller, F. Dreisbach, R. Glaeser, R. Staudt, Microporous Mesoporous Mater. 138 (2011) 140–148.
- [48] S. Sircar, AIChE J. 47 (5) (2001) 1169–1176.
- [49] Y. Gucbilmez, T. Dogu, S. Balci, Catal. Today 100 (2005) 473–477.
- [50] G.E. Froudakis, Nano Lett. 1 (2001) 531–533.
- [51] K.R.S. Chandrakumar, S.K. Ghosh, Nano Lett. 8 (2008) 13–19.
- [52] M. Hirscher, B. Panella, B. Schmitz, Microporous Mesoporous Mater. 129 (2010) 335–339.
- [53] E. Poirier, A. Dailly, Energy Environ. Sci. 2 (2009) 420–425.
- [54] M. Zielinski, R. Wojcieszak, S. Monteverdi, M. Mercy, M.M. Bettahar, Int. J. Hydrogen Energy 32 (2007) 1024–1032.
- [55] M. Bastos-Neto, C. Patzschke, M. Lange, J. Mollmer, A. Moller, S. Fichtner, C. Schrage, D. Lassig, J. Lincke, R. Staudt, H. Krautscheid, R. Glaser, Energy Environ. Sci. 5 (2012) 8294–8303.